Taylor & Francis
Taylor & Francis Group

Science and Technology of Advanced Materials

ISSN: 1468-6996 (Print) 1878-5514 (Online) Journal homepage: www.tandfonline.com/journals/tsta20

Synthesis and thermal stability of topological semimetal *R*MnSb$_2$ (*R* = Yb, Sr, Ba, Eu)

Shuo Liu, Airan Li, Xiaowen Hao, Mengzhao Chen, Yi Huang, Yinde Yu, Chin-Wei Wang, Qingyong Ren, Tiejun Zhu & Chenguang Fu

To cite this article: Shuo Liu, Airan Li, Xiaowen Hao, Mengzhao Chen, Yi Huang, Yinde Yu, Chin-Wei Wang, Qingyong Ren, Tiejun Zhu & Chenguang Fu (28 May 2025): Synthesis and thermal stability of topological semimetal *R*MnSb$_2$ (*R* = Yb, Sr, Ba, Eu), Science and Technology of Advanced Materials, DOI: 10.1080/14686996.2025.2512702

To link to this article: https://doi.org/10.1080/14686996.2025.2512702

Publisher: Taylor & Francis & The Author(s). Published by National Institute for Materials Science in partnership with Taylor & Francis Group.

Journal: *Science and Technology of Advanced Materials*

DOI: 10.1080/14686996.2025.2512702

Synthesis and thermal stability of topological semimetal *R*MnSb$_2$ (*R* = Yb, Sr, Ba, Eu)

Shuo Liu[a], Airan Li[a], Xiaowen Hao[b,c], Mengzhao Chen[a], Yi Huang[a], Yinde Yu[b,c], Chin-Wei Wang[d], Qingyong Ren[b,c,*], Tiejun Zhu[a,*] Chenguang Fu[a,*]

[a]State Key Laboratory of Silicon and Advanced Semiconductor Materials, School of Materials Science and Engineering, Zhejiang University, Hangzhou 310058, China

[b]Spallation Neutron Source Science Center, Dongguan 523803, China

[c]Institute of High Energy Physics, Chinese Academy of Sciences, Beijing 100049, China

[d]Neutron Group, National Synchrotron Radiation Research, Hsinchu 300092, Taiwan

[*]Email: chenguang_fu@zju.edu.cn; zhutj@zju.edu.cn; renqy@ihep.ac.cn

Abstract

YbMnSb$_2$, a topological semimetal with an exotic band structure, has recently been found to exhibit potential thermoelectric transport properties in its single-crystalline formality. The fabrication of polycrystals, which have the advantages of easy synthesis and doping tunability, will advance the transport studies of YbMnSb$_2$ but face challenges. Here, we found that the polycrystalline YbMnSb$_2$, synthesized using the conventional melting method, unexpectedly exhibits obvious impurities due to the competing phase YbMn$_2$Sb$_2$. To avoid the high-temperature synthesis, high-quality polycrystalline bulk YbMnSb$_2$, as well as three other *R*MnSb$_2$ (*R* = Sr, Ba, Eu), were successfully prepared by mechanical alloying followed by spark plasma sintering. Based on the high-quality polycrystalline samples, it was discovered that YbMnSb$_2$ reacts with oxygen during heating in the presence of small amounts of oxygen, resulting in MnSb, Yb$_2$O$_3$, and Sb. A similar oxidation phenomenon also occurs for the other *R*MnSb$_2$. This work provides a feasible method for synthesizing high-quality *R*MnSb$_2$ polycrystals, which should also be suitable for the other isostructural topological semimetals, paving the way for future studies of their transport properties.

Keywords
Topological semimetals, polycrystals, thermal stability, YbMnSb$_2$

1. Introduction

Solid-state thermoelectric (TE) technology, based on TE materials, offers a promising solution for energy harvesting and refrigeration.[1-6] The conversion efficiency of a TE material is usually gauged by the dimensionless figure of merit zT, which is expressed as $zT = S^2\sigma T/ (\kappa_e + \kappa_L)$, where S, σ, T, κ_e, and κ_L are the Seebeck coefficient, electrical conductivity, absolute temperature, electronic thermal conductivity, and lattice thermal conductivity, respectively.[7] To enhance the zT of a TE material, the optimization of the electrical power factor (PF = $S^2\sigma$) is as important as suppressing the κ_L, the latter can typically be achieved by using the multiscale phonon scattering strategy.[8] The electronic band structure is crucial in determining the S and σ of solid materials. Good TE materials generally have the characteristics of multiple converged electronic bands and/or anisotropic Fermi surfaces.[2,9-13] Owing to that, a few band engineering strategies have been proposed in the past years, aiming at the optimization of PF.[14,15]

For conventional TE semiconductors, the carriers involved in the electrical transport are those situated near the Fermi level E_F, usually several k_BT (k_B is the Boltzmann constant) above and below the E_F. Thus, the fine characteristics of band structure near the Fermi level E_F play a key role in determining the TE transport properties. Conventionally, high-performance TE materials are generally narrow bandgap semiconductors with the position of E_F located near the edge of conduction or valence bands.[16] In recent years, emerging topological semimetals with exotic electronic structures near the E_F have been discovered,[17-20] which provide new material platforms to explore emerging physical phenomena and potential TE materials.[21-25]

RMnX_2-type Zintl phase compounds, in which R represents an alkali metal or alkaline earth metal elements and X represents Sb, Bi, P, and As,[26] have attracted considerable research attention due to their unique electronic structure that couples with magnetism and topology.[27] Previously, SrMnBi$_2$[28] and YbMnBi$_2$[29,30] have been recognized as topological semimetals with magnetic order.[31] For

R$MnSb_2$-based materials, the square mesh structure of Sb is capable of delivering highly anisotropic Dirac dispersion,[32] for instance, in $CaMnSb_2$,[33] $SrMnSb_2$,[27] and $BaMnSb_2$.[34] Similarly, the first-principle calculations on $YbMnSb_2$ also revealed an anisotropic Dirac band characteristic.[35] Besides, $YbMnSb_2$ single crystal was experimentally found exhibiting a large anisotropy in the electrical and thermal transport properties when the carriers transport along the *ab*-plane and the *c*-axis directions, respectively.[36] The highly dispersive Dirac bands, coexisting with the regular band, lead to a maximum PF of 2.1 mW m^{-1} K^{-2} at 300 K in ab-plane, which approaches that of Bi_2Te_3 single crystal, indicating the TE potential of $YbMnSb_2$.

However, previous studies on $YbMnSb_2$, as well as $RMnX_2$, were mainly focused on single crystals,[35,37-39] which were typically grown using the self-flux method. The length of the as-grown single crystals is generally around several millimeters, making it difficult to explore the TE potential, particularly above room temperature, due to the general requirement of larger samples for transport properties measurements. Besides, the impurity phases might appear after the heating test, as found in the temperature-dependent magnetic susceptibility test of single crystalline $SrMnSb_2$[40]. For $YbMnSb_2$, the temperature-dependent magnetization curve also presents an upturn at low temperatures,[39] indicating a possible ferromagnetic impurity phase.[37] In this context, exploring methods to grow high-quality polycrystals with larger dimensions will facilitate the investigations of the TE potential of $YbMnSb_2$ and related $RMnX_2$-based topological semimetals.

In this work, we find that $YbMnSb_2$ polycrystals, synthesized using the conventional melting method, unexpectedly exhibit obvious impurities due to the competing phase $YbMn_2Sb_2$. Instead, high-quality bulk $YbMnSb_2$ could be successfully synthesized via high-energy mechanical alloying followed by spark plasma sintering (SPS). Further analysis revealed that during heating, a phase transition occurs even at low oxygen content, producing impurities, including the ferromagnetic MnSb. This work paves the way for exploring the TE potential of

$YbMnSb_2$, as well as the other *R*MnX_2-based topological semimetals, using high-quality polycrystals.

2. Methods

Synthesis

$YbMnSb_2$ single crystals were prepared using the self-flux method. High purity elements, Yb (pieces, 99.9%), Mn (blocks, 99.95%), and Sb (blocks, 99.999%) were weighted with a molar ratio of Yb: Mn: Sb = 1: 1: 4, then loaded into Al_2O_3 crucibles with sieves and sealed in quartz tubes under vacuum. Tubes were heated to 1323 K and dwelled for 48 hours, then slowly cooled down to 923 K at a rate of 2 K/h and centrifugated to remove excess Sb elements. For fabricating polycrystalline $YbMnSb_2$, two methods were used, i.e., conventional melting followed by spark plasma sintering SPS (named: M+SPS) and mechanical ball milling (named: BM+SPS). For the M+SPS method, starting elements were weighted according to the stoichiometric composition and loaded into a quartz tube. The tube was heated to 1323 K, dwelled for 48 hours, and then cooled to room temperature in 24 hours. The obtained ingot was manually ground and loaded into a graphite die (diameter: 12.7 mm) and then compacted by SPS (SPS-1050; Sumitomo Coal Mining Co.) under 823 K and 70 MPa in a vacuum for 10 min. For the BM+SPS method, high-purity elements, Yb (pieces, 99.9%), Mn (blocks, 99.95%), and Sb (blocks, 99.999%) were weighted according to the stoichiometric composition and then mechanically milled (SPEX-8000D, PYNN Corporation) for different periods under argon protection. The obtained fine powders were compacted by SPS under 823 K and 70 MPa in a vacuum for 10 min. The samples subjected to SPS after ball milling (BM) for 1, 2, 4, and 8 h were named BM for 1, 2, 4, and 8 h, respectively. The same BM (for 2 h) +SPS method was also used for synthesizing polycrystalline *R*MnSb_2, with high raw elements of Sr (pieces, 99%), Ba (pieces, 99%), Eu (pieces, 99.9%) Mn (blocks, 99.95%), and Sb (blocks, 99.999%).

Characterization

The single crystals of $YbMnSb_2$ were checked at room temperature by the Laue X-ray diffraction (XRD) method (Photonic Science Limited). The powders obtained by grinding single crystals were characterized by XRD (PANalytical/Areis diffractometer) and neutron powder diffraction. Temperature-dependent crystal structure, magnetic structure, and intrinsic lattice change were determined by in-situ neutron powder diffraction using the High-Intensity Powder Diffractometer, Wombat, at the Australian Nuclear Science and Technology Organization (ANSTO) in Australia. Neutron Diffraction patterns were collected over 10 ~ 450 K with a wavelength of 2.42 Å, and then the crystal and magnetic structures were analyzed with Rietveld refinement and irreducible representation methods using the Fullprof suite. The variable temperature XRD patterns (D8 DISCOVER in-situ XRD of BRUKER) were further carried out from 323 K to 873 K. The composition of the bulks was identified by electron probe microanalysis (EPMA, JOEL, JXA-8100) with a wavelength-dispersive spectroscope (WDS). Differential scanning calorimeter (DSC, TA, Q200) measurements were performed in argon flux with a heating rate of 10 $K \cdot min^{-1}$.

Measurements

The σ and S above room temperature were measured simultaneously from 300 K to 573 K using the commercial LSR-3 (Linseis) system. The thermal conductivity was calculated from $\kappa = DC_P\rho$, where D was the thermal diffusivity measured by the laser flash method using Netzsch LFA 457, C_P was the specific heat capacity estimated from the Dulong-Petit law, and ρ was the density of samples measured by Archimedes' method. The magnetic properties were measured with the vibrating sample magnetometer (VSM) option of the Physical Property Measurement System (PPMS). The electrical transport properties below room temperature were measured by the Cryogenic Mini low-temperature physical property measurement system (Cryogenic Limited).

3. Results and Discussion

Experimentally, to explore the TE potential of $YbMnSb_2$, it is paramount to have high-quality samples. For synthesizing Zintl phase compounds, vacuum melting at high temperatures is one of the most commonly used methods, which has been successfully used in the emerging Mg_3Sb_2 and RMg_2X_2 compounds.[41,42] In this work, we first employ the vacuum melting method to synthesize polycrystalline $YbMnSb_2$. The as-melted ingots were ground and examined by XRD analysis. As presented in Figure 1a, in addition to the diffraction peaks that can be indexed to be the $YbMnSb_2$ phase, there are also diffraction peaks that suggest the existence of the $YbMn_2Sb_2$ phase. It is worth noting that this does not happen occasionally but always occurs when repeating the experiments. To improve the phase purity, the as-melted ingot was ground and then loaded into a graphite die and compacted by SPS. Similarly, except for the main phase $YbMnSb_2$, there is still a coexistence of heterogeneous phase $YbMn_2Sb_2$ in the bulk polycrystalline sample fabricated using the M+SPS method (Fig. 1a). Microstructure analysis using EPMA was further carried out (Fig. 1b), which shows indeed a coexistence of $YbMnSb_2$ and $YbMn_2Sb_2$ in the polycrystalline bulk, consistent with the XRD analysis (Fig. 1a). The sample shows anisotropic electrical properties (Fig. S1), similar to those of the single crystals grown using self-flux method [36].

The crystal structures of $YbMnSb_2$ and $YbMn_2Sb_2$ are presented in Fig. 1c and 1d, respectively. $YbMnSb_2$ crystallized in a tetragonal lattice with a space group $P4/nmm$ (Fig. 1c). It consists of a two-dimensional Sb-conducting layer, a Yb^{2+} cation layer, and an $MnSb_4$ anion-cluster layer stacked on top of each other. Each manganese atom is surrounded by four Sb atoms in the anion cluster, forming a tetrahedron. The Sb atoms are arranged to form a square mesh structure mainly consisting of covalent bonds, which can provide a fast channel for the migration of carriers.[36] $YbMn_2Sb_2$ crystallizes in a trigonal symmetry (Fig. 1d).[43] Mn and Sb form anionic clusters, and Yb forms a cationic layer. Thermodynamically, both $YbMnSb_2$ and $YbMn_2Sb_2$ present negative formation energy, i.e., -0.158 eV/atom for $YbMnSb_2$ and -0.186 eV/atom for $YbMn_2Sb_2$. The formation energy of $YbMn_2Sb_2$ is even lower than that of $YbMnSb_2$. During the fabrication of $YbMnSb_2$ using vacuum melting, even though a stoichiometric ratio of 1:1:2 was employed in the nominally designed composition, there is still a high probability that $YbMn_2Sb_2$, as a competing phase, can be formed due to its lower formation energy.

To further examine this, $YbMnSb_2$ single crystals were grown using a self-flux method with Sb as the flux, as previously reported.[44] The crystals exhibit clear cleavage surfaces (Fig. S2), indicating their high crystallinity and orientation, which were confirmed through XRD analysis (Fig. S3) and Laue diffraction (Fig. S2). It is important to note that both XRD and Laue diffraction were performed on the surface of the crystal. To further examine the composition and quality inside the crystals, the single crystals were ground into powders for neutron powder diffraction (NPD) and XRD analysis.

NPD is a valuable tool for acquiring unique magnetic information, which can be directly used to study the microstructure and magnetic ground state of solid materials. As $YbMnSb_2$ belongs to antiferromagnetic (AFM) material, the acquisition of NPD data at different temperatures is necessary to acquire the AFM structural information. An in-situ NPD study was performed for powder grounded from the single crystal on the Wombat Instrument at ANSTO, Australia. Rietveld refinements of neutron diffraction patterns at 300 K and 450 K are presented in Fig. 2a. The NPD pattern at 300 K reveals the presence of both Sb and $YbMn_2Sb_2$ impurities, besides the main phase of $YbMnSb_2$. The Sb impurity might originate from the unremoved flux, while the existence of $YbMn_2Sb_2$ indicates that it is a stable competing phase that can still exist during the flux growth of single-crystal $YbMnSb_2$. It is further demonstrated that even if a single crystal has a very good crystalline quality on the surface, it does not guarantee a homogeneous and pure composition inside, as also supported by the powder XRD pattern (Fig. S4). The diffraction peak at 35° in the NPD pattern at 300 K is higher than it is at 450 K, and the gap between the peak intensities is caused by (±1 0 1) & (0 ±1 1) magnetic diffraction peaks. Furthermore, around 32.3°, there is a (0 1 0) magnetic peak in the NPD pattern at 300 K, which disappears at 350 K, indicating the AFM structure of $YbMnSb_2$. The refinement results show that the arrangement of Mn^{2+} is the *C*-type AFM (Fig S5a) order structure at 300 K, in which all Mn spins lie parallel to the c-axis, consistent with the previous report.[39]

To better illustrate the temperature-dependent variation of magnetic peaks, NPD results at different temperatures are presented in Fig. 2b. The magnetic peaks of $YbMnSb_2$ diminish around 350 K, similar to the result obtained from the temperature-dependent magnetization curves in the literature.[45] Both Fig. 2b and Fig. 2c show a sudden change in magnetization around T_N = 350 K, indicative of a change in the magnetic structure of $YbMnSb_2$. In addition to the observed AFM-paramagnetic transition in $YbMnSb_2$, we also observed a small, inconspicuous peak at around 37.5°. Combining the isothermal contour image of the zero-field neutron diffraction pattern, it can be observed that the peak disappears at around 120 K (Fig. 2c), which corresponds to the Néel temperature of $YbMn_2Sb_2$.[46]

As analyzed above, $YbMn_2Sb_2$, as a competing phase, seems to be inevitable for synthesizing both single-crystalline and polycrystalline $YbMnSb_2$ when experiencing the liquid melting process. Differently, high-energy mechanical ball milling followed by hot press or SPS is an effective means for obtaining polycrystalline bulk samples without experiencing the high-temperature liquid-melting process, which might work for synthesizing high-quality $YbMnSb_2$. To ensure reproducibility, we tried to synthesize $YbMnSb_2$ samples by ball-milling with varied durations, i.e., 1, 2, 4, and 8 hours, followed by SPS. The XRD patterns for the as-prepared bulk $YbMnSb_2$ samples are shown in Fig. 3a. It can be observed that only the sample ground for 1 hour exhibits a slight Sb impurity phase. With increased BM time, no obvious impurity phases are observed, indicating a good phase purity. Thus, the combination of BM and SPS processes could effectively prevent the formation of competing and impurity phases, resulting in high-quality $YbMnSb_2$ polycrystalline samples, as further validated by the microstructural and EPMA compositional characterization. As shown in Fig. 3b-3e, the matrix composition is homogeneous. In addition, the SEM images on the fractured surfaces reveal that grain size decreases with increasing BM time (Fig. S6).

The obtained high-quality $YbMnSb_2$ polycrystals provide the opportunity to investigate the thermal behavior before carrying out the TE properties investigations. DSC measurements were conducted in argon flux on the powders ground from the $YbMnSb_2$ bulk sample (BM for 4 h). The DSC results revealed endothermic peaks around 827 K and 1103 K during the heating process (Fig. 4a). To further investigate the phase changes during heating, in-situ XRD was performed under a vacuum condition of 10^{-1} Pa provided by a mechanical pump. With increasing temperature, the sample composition changes, and $YbMnSb_2$ eventually transforms into other phases (Fig. 4b).

According to the thermal analysis above, an obvious phase transition occurs in $YbMnSb_2$ during heating in the presence of a small amount of air. During gradual heating, the oxidation of $YbMnSb_2$ will occur and the final products become Yb_2O_3, MnSb, and Sb (Fig. 4b). Such an oxidation process is irreversible as the reaction products remain when the temperature drops back to room temperature. Therefore, it is hypothesized that the following oxidation reaction occurs: $4YbMnSb_2 + 3O_2 \rightarrow 2Yb_2O_3 + 4MnSb + 4Sb$. Since Yb_2O_3 has a high melting point of about 2623 K and Sb has a melting point of 903 K (corresponding to the T_3 in Fig. 4a), it does not correspond to the two endothermic peaks mentioned previously. Thus, the phenomenon appearing in Fig. 4a may be related to MnSb. To further elucidate the phenomena observed in Fig. 4a, a high-quality MnSb sample was further prepared (Fig. S7). The DSC of MnSb also revealed two endothermic peaks during the heating process (Fig. 4c). By further analysis, it can be speculated that the endothermic peak at 807 K corresponds to the peritectic reaction “MnSb → Mn_xSb + Liquid” (Fig 4c).[47] The wide endothermic peak below 1103 K indicates the melting process, corresponding to the endothermic peak of Fig. 4a.

To examine the phases formed during heating, annealing experiments were conducted in different atmospheres in a sealed quartz tube on powders of $YbMnSb_2$ (Fig. 4d). Under an argon atmosphere, the phase of the sample remains unchanged. When annealing under a low vacuum of around 10^{-2} Pa, part of the sample transforms into Yb_2O_3, MnSb, and Sb, consistent with the results of in-situ XRD with different temperatures. Additionally, *M-H* tests were further conducted on the samples before and after annealing (Fig. S8). Before annealing, the sample exhibited AFM properties and low magnetization. After annealing, magnetic hysteresis and higher magnetization occur,[48] indicating ferromagnetic (FM) properties. The EPMA results of the annealed sample (Fig. S9, Table S1) reveal the react production of $YbMnSb_2$, which was replaced by a mixture of several new phase. The white regions correspond to Yb_2O_3 and Sb, while the gray regions are MnSb. The existence of ferromagnetic MnSb could also explain the FM signals observed in previous studies.[39] When annealed under air conditions, it oxidizes more completely by producing various oxides of Yb, Sb, and Mn. These results indicate that $YbMnSb_2$ is not stable when heated up under an oxygen atmosphere. It is worth noting that $YbMnSb_2$ powders left in the air for several weeks remain unchanged (Fig. S10), indicating the oxidation process is slow at ambient temperature.

It is worth noting that the BM+SPS method can also be used to synthesize the other high-quality RMnSb$_2$ (here, R = Sr, Ba, Eu) compounds. The XRD patterns for the as-prepared samples are shown in Fig. 5a-5c, which matches well with the simulated ones. The DSC results (Fig. S11) also revealed endothermic peaks during the heating process, similar to that of $YbMnSb_2$. As Fig. 5a-5c shows, similar oxidation phenomena also occur for the studied RMnSb$_2$, indicating that they are not stable when heating up under the condition of oxygen. Therefore, one can conclude that preparing high-purity $RMnSb_2$ samples requires oxygen-isolated conditions combined with the avoided formation of competing phase RMn$_2$Sb$_2$.

Figure 6 presents the temperature dependence of TE properties for $YbMnSb_2$ bulk samples. As the temperature increases above 300 K, the bipolar conduction becomes more pronounced, leading to the rapidly increased σ and reduced absolute S (Fig. 6a). The temperature-dependent σ for all four samples remains similar. At the same time, the S shows substantial differences and even p-to-n transition with increasing BM time, which is probably related to the defects induced during the BM process that slightly change the dominated carrier concentration and type. In terms of thermal transport properties, increasing BM time reduces grain size and increases grain boundaries (Fig. S4), leading to a decrease in the lattice thermal conductivity (Fig. 6b). The PF of $YbMnSb_2$ (BM for 2 h) presents the maximum value at room temperature, which is about 0.65 mW m^{-1} K^{-2} (Fig. 6c), resulting in a maximum *zT* value of about 0.07 at 300 K.

4. Summary

In summary, a comprehensive study on the phase structure of $YbMnSb_2$ synthesized using different methods and how to obtain high-quality samples was carried out. It is found that the polycrystalline $YbMnSb_2$, synthesized using the conventional melting method, unexpectedly exhibits obvious impurities due to the existence of the competing phase $YbMn_2Sb_2$. To avoid the high-temperature synthesis, high-quality polycrystalline $YbMnSb_2$, as well as three other RMnSb$_2$ (R = Sr, Ba, Eu) bulk samples, were successfully prepared by mechanical alloying followed by spark plasma sintering. It was further discovered that $YbMnSb_2$ reacts with oxygen during heating in the presence of small amounts of oxygen, resulting in MnSb, Yb_2O_3, and Sb. A maximum power factor of 0.65 mW m^{-1} K^{-2} was obtained at room temperature for polycrystalline $YbMnSb_2$. These results highlight the method to synthesize high-quality RMnSb$_2$ polycrystals and their thermal instability in the condition of oxygen, which will pave the way for future studies of their transport properties.

Acknowledgments

This work was supported by the National Key Research and Development Program of China (Nos. 2019YFA0704900), and the National Natural Science Foundation of China (Nos. 52471239, 92163203, 12474024, 52401252). Q.R. acknowledges the beam time granted by ANSTO.

Disclosure statement

No potential conflict of interest was reported by the authors.

Author contributions

Shuo Liu: Data curation, Formal analysis, Validation, Investigation, Writing-original draft, Writing-review & editing; **Airan Li**: Methodology, Formal analysis; **Xiaowen Hao**: Data curation, Formal analysis, Writing-review & editing; **Mengzhao Chen**: Data curation; **Yi Huang**: Data curation; **Yinde Yu**: Formal analysis; **Chin-Wei Wang**: Data curation, Writing-review & editing; **Qingyong Ren**: Data curation, Writing-review & editing; **Tiejun Zhu**: Investigation, Project administration, Supervision, Writing-review & editing; **Chenguang Fu**: Formal analysis, Validation, Investigation, Project administration, Supervision, Writing-review & editing.

References

[1] He J, Tritt TM. Advances in thermoelectric materials research: Looking back and moving forward. Science. 2017;357(6358):eaak9997. doi: 10.1126/science.aak9997

[2] Zhu T, Liu Y, Fu C, et al. Compromise and synergy in high-efficiency thermoelectric materials. Adv. Mater. 2017;29(14):1605884. doi: 10.1002/adma.201605884

[3] Petsagkourakis I, Tybrandt K, Crispin X, et al. Thermoelectric materials and applications for energy harvesting power generation. Sci. Technol. Adv. Mater. 2018;19(1):836-862. doi: 10.1080/14686996.2018.1530938

[4] Bano S, Chetty R, Babu J, et al. $Mg_3(Sb,Bi)_2$-based materials and devices rivaling bismuth telluride for thermoelectric power generation and cooling. Device. 2024;2(7):100408. doi: 10.1016/j.device.2024.100408

[5] Ma D, Ma Y, Ma J, et al. Energy conversion materials need phonons. The Innovation. 2024;5(6):100709. doi: 10.1016/j.xinn.2024.100709

[6] Wang Y, Li A, Hong Y, et al. Iterative sublattice amorphization facilitates exceptional processability in inorganic semiconductors. Nat. Mater. 2025:1-9. doi: 10.1038/s41563-024-02112-7

[7] Snyder GJ, Toberer ES. Complex thermoelectric materials. Nat. Mater. 2008;7(2):105-114. doi: 10.1038/nmat2090

[8] Fu C, Sun Y, Felser C. Topological thermoelectrics. APL Mater. 2020;8(4): 040913. doi: 10.1063/5.0005481

[9] Pei Y, Shi X, LaLonde A, et al. Convergence of electronic bands for high performance bulk thermoelectrics. Nature. 2011;473(7345):66-69. doi: 10.1038/nature09996

[10] Zhao L, Tan G, Hao S, et al. Ultrahigh power factor and thermoelectric performance in hole-doped single-crystal SnSe. Science. 2016;351(6269):141-144. doi: 10.1126/science.aad3749
[11] Li A, Hu C, He B, et al. Demonstration of valley anisotropy utilized to enhance the thermoelectric power factor. Nat. Commun. 2021;12(1):5408. doi: 10.1038/s41467-021-25722-0
[12] Liu J, Li A, Fu C, et al. Band anisotropy in thermoelectric materials. The Innovation Materials. 2023;1(1):100004. doi: 10.59717/j.xinn-mater.2023.100004
[13] Hu C, Gao Z, Zhang M, et al. Intrinsic conductivity as an indicator for better thermoelectrics. Energy Environ. Sci. 2023;16(11):5381-5394. doi: 10.1039/D3EE02167J
[14] Pei Y, Wang H, Snyder GJ. Band engineering of thermoelectric materials. Adv. Mater. 2012;24(46):6125-6135. doi: 10.1002/adma.201202919
[15] Yao W, Zhang Y, Lyu T, et al. Two-step phase manipulation by tailoring chemical bonds results in high-performance GeSe thermoelectrics. The Innovation. 2023;4(6):100522. doi: 10.1016/j.xinn.2023.100522
[16] Zhang M, Gao Z, Lou Q, et al. Achieving high carrier mobility and thermal stability in plainified rhombohedral GeTe thermoelectric materials with $zT > 2$. Adv. Funct. Mater. 2024;34(6):2307864. doi: 10.1002/adfm.202307864
[17] Soluyanov AA, Gresch D, Wang Z, et al. Type-II Weyl semimetals. Nature. 2015;527(7579):495-498. doi: 10.1038/nature15768
[18] Xu S, Belopolski I, Alidoust N, et al. Discovery of a Weyl fermion semimetal and topological Fermi arcs. Science. 2015;349(6248):613-617. doi: 10.1126/science.aaa929
[19] Yan B, Felser C. Topological materials: Weyl semimetals. Annu. Rev. Condens. Matter Phys. 2017;8:337-354. doi: 10.1146/annurev-conmatphys-031016-025458
[20] Kriener M, Koretsune T, Arita R, et al. Enhancement of the thermoelectric figure of merit in the Dirac semimetal Cd_3As_2 by band-structure and -filling control. Sci. Technol. Adv. Mater. 2024;25(1):2412971. doi: 10.1080/14686996.2024.2412971
[21] Sun P, Kumar KR, Lyu M, et al. Generic Seebeck effect from spin entropy. The Innovation. 2021;2(2):100101. doi: 10.1016/j.xinn.2021.100101
[22] Sun Z, Wang H, Wang A, et al. Large Thermopower Enhanced by Spin Entropy in Antiferromagnet $EuMnSb_2$. Adv. Funct. Mater. 2022, 32(33): 2202188. doi: 10.1002/adfm.202202188
[23] Yadav S, Kumar BA, Guin SN. Topological transverse thermoelectrics: A new way forward? The Innovation. 2023;4(6):100530. doi: 10.1016/j.xinn.2023.100530
[24] Chen M, Wang J, Liu K, et al. Topological Heusler Magnets-Driven High-Performance Transverse Nernst Thermoelectric Generators. Adv. Energy Mater. 2024, 14(21): 2400411. doi: 10.1002/aenm.202400411
[25] Toriyama MY, Snyder GJ. Topological insulators for thermoelectrics: A

perspective from beneath the surface. The Innovation. 2025;6(3):100782. doi: 10.1016/j.xinn.2024.100782

[26] Klemenz S, Lei S, Schoop LM. Topological Semimetals in Square-Net Materials. Annu. Rev. Mater. Res. 2019;49:185-206. doi: 10.1146/annurev-matsci-070218-010114

[27] Liu J, Hu J, Zhang Q, et al. A magnetic topological semimetal Sr_{1-y} Mn_{1-z} Sb_2 (y, $z < 0.1$). Nat. Mater. 2017;16(9):905-910. doi: 10.1038/NMAT4953

[28] Zhang A, Liu C, Yi C, et al. Interplay of Dirac electrons and magnetism in $CaMnBi_2$ and $SrMnBi_2$. Nat. Commun. 2016;7(1):13833. doi: 10.1038/ncomms13833

[29] Borisenko S, Evtushinsky D, Gibson Q, et al. Time-reversal symmetry breaking type-II Weyl state in $YbMnBi_2$. Nat. Commun. 2019;10(1):3424. doi: 10.1038/s41467-019-11393-5

[30] Pan Y, Le C, He B, et al. Giant anomalous Nernst signal in the antiferromagnet $YbMnBi_2$. Nat. Mater. 2022;21(2):203-209. doi: 10.1038/s41563-021-01149-2

[31] Yan B, Felser C. Topological materials: Weyl semimetals. Annu. Rev. Mater. Res. 2017;8(1):337-354. doi: 10.1146/annurev-matsci-070218-010114

[32] Boothroyd AT. Topological electronic bands in crystalline solids. Contemp. Phys. 2022;63(4):305-327. doi: 10.1080/00107514.2023.2251764

[33] He J, Fu Y, Zhao L, et al. Quasi-two-dimensional massless Dirac fermions in $CaMnSb_2$. Phys. Rev. B. 2017;95(4):045128. doi: 10.1103/PhysRevB.95.045128

[34] Liu J, Yu J, Ning J, et al. Spin-valley locking and bulk quantum Hall effect in a noncentrosymmetric Dirac semimetal $BaMnSb_2$. Nat. Commun. 2021;12(1):4062. doi: 10.1038/s41467-021-24369-1.

[35] Kealhofer R, Jang S, Griffin SM, et al. Observation of a two-dimensional Fermi surface and Dirac dispersion in $YbMnSb_2$. Phys. Rev. B. 2018;97(4):045109. doi: 10.1103/PhysRevB.97.045109

[36] Pan Y, Fan F, Hong X, et al. Thermoelectric Properties of Novel Semimetals: A Case Study of $YbMnSb_2$. Adv. Mater. 2021;33(7):2003168. doi: 10.1002/adma.202003168.

[37] Wang Y, Xu S, Sun L, et al. Quantum oscillations and coherent interlayer transport in a new topological Dirac semimetal candidate $YbMnSb_2$. Phys. Rev. Mater. 2018;2(2):021201. doi: 10.1103/PhysRevMaterials.2.021201

[38] Qiu Z, Le C, Liao Z, et al. Observation of a topological nodal-line semimetal in $YbMnSb_2$ through optical spectroscopy. Phys. Rev. B. 2019;100(12):125136. doi: 10.1103/PhysRevB.100.125136

[39] Soh JR, Tobin SM, Su H, et al. Magnetic structure of the topological semimetal $YbMnSb_2$. Phys. Rev. B. 2021;104(16):161103. doi: 10.1103/PhysRevB.104.L161103

[40] Liu Y, Ma T, Zhou L, et al. Crystal growth, microstructure, and physical properties of $SrMnSb_2$. Phys. Rev. B. 2019;99(5):054435. doi: 10.1103/PhysRevB.99.054435

[41] Li A, Nan P, Wang Y, et al. Chemical stability and degradation mechanism of $Mg_3Sb_{2-x}Bi_x$ thermoelectrics towards room-temperature applications. Acta Mater. 2022;239:118301. doi: 10.1016/j.actamat.2022.118301

[42] Wang Q, Liu K, Su Y, et al. High thermoelectric performance and anisotropy studies of n-type Mg_3Bi_2-based single crystal. Acta Mater. 2023;255:119028. doi: 10.1016/j.actamat.2023.119028

[43] Morozkin A, Isnard O, Henry P, et al. Synthesis and magnetic structure of the $YbMn_2Sb_2$ compound. J. Alloys Compd. 2006;420(1-2):34-36. doi: 10.1016/j.jallcom.2005.10.051

[44] Baranets S, Bobev S. Transport properties and thermal behavior of $YbMnSb_2$ semimetal above room temperature. J. Solid State Chem. 2021;303:122467. doi: 10.1016/j.jssc.2021.122467

[45] Nirmala R, Morozkin A, Suresh K, et al. Magnetism and transport in $YbMn_2Sb_2$. J. Appl. Phys. 2005;97(10). doi: 10.1063/1.1851815

[46] Munevar J, Arantes F, Mendonça-Ferreira L, et al. Study of the magnetic properties of $YbMn_2Sb_2$ single crystals by μSR. Journal of Magnetism and Magnetic Materials. 2021;537:168149. doi: 10.1016/j.jmmm.2021.168149

[47] Polash MMH, Mohaddes F, Rasoulianboroujeni M, et al. Magnon-drag thermopower in antiferromagnets ferromagnets. J. Mater. Chem. C. 2020;8(12):4049-4057. doi: 10.1039/c9tc06330g

[48] Liu S, Chen M, Fu C, et al. The Interplay of Magnetism and Thermoelectricity: A Review. Adv. Phys. Res. 2023:2(9):2300015. doi: 10.1002/apxr.202300015

Figures and captions

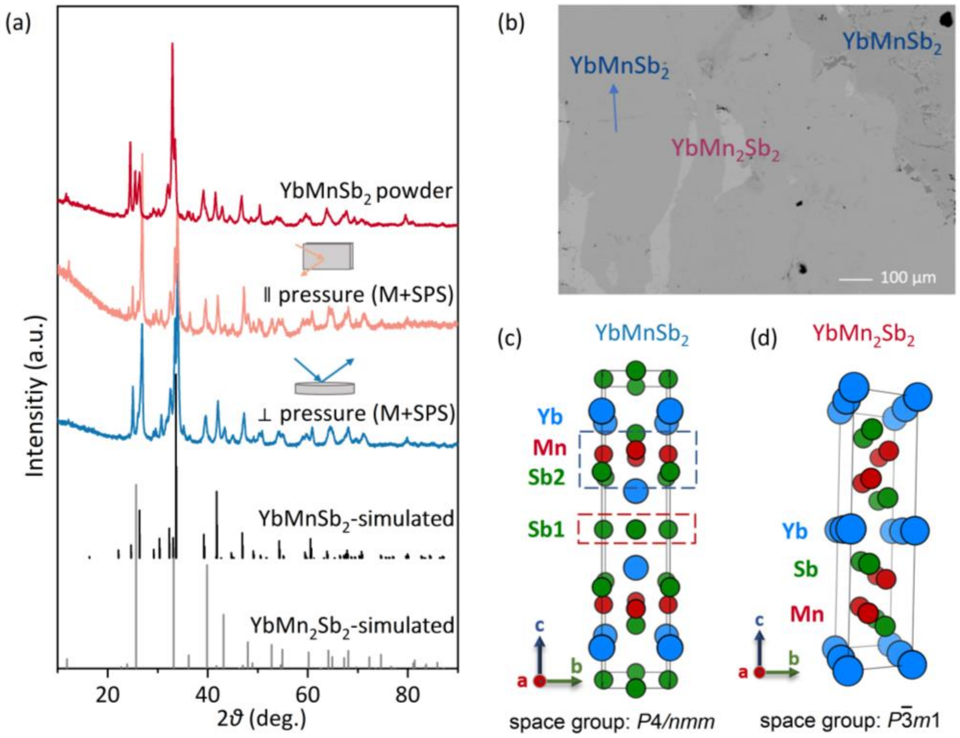

Figure 1. (a) XRD patterns for the YbMnSb$_2$ powders ground from the as-melted ingot (dark red) and bulk polycrystalline YbMnSb$_2$ samples fabricated using the M+SPS method in the direction parallel (light red) and perpendicular to the pressure (light blue), respectively. (b) Backscattered electron (BSE) images of polycrystalline YbMnSb$_2$ sample fabricated using the M+SPS method; The crystal structure of (c) YbMnSb$_2$ and (d) YbMn$_2$Sb$_2$.

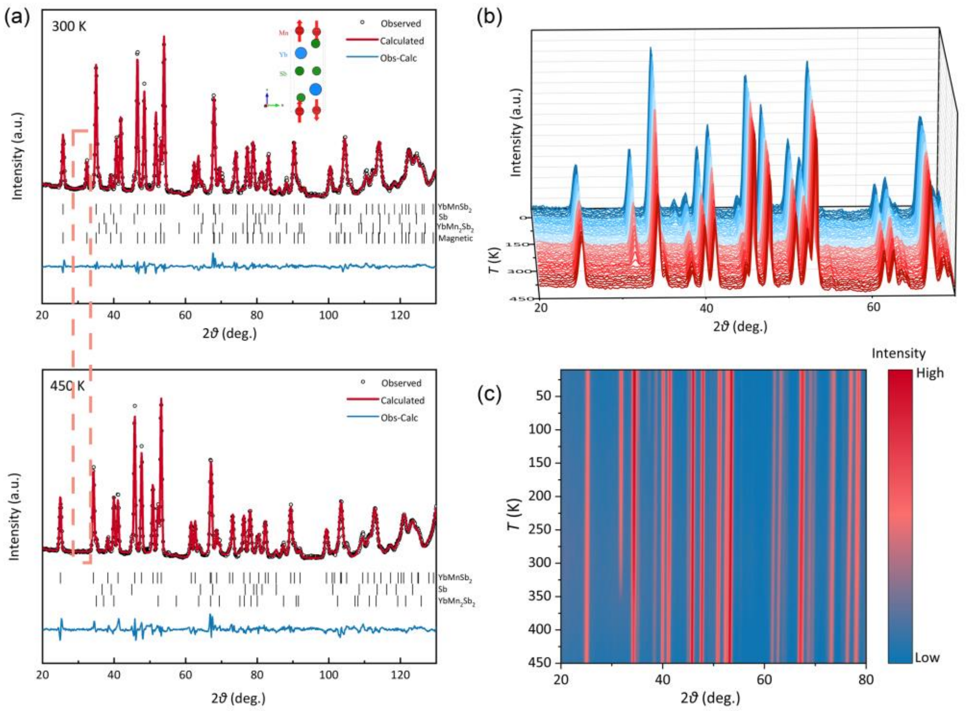

Figure 2. (a) Rietveld refinements of neutron diffraction patterns at selected temperatures, 300 K and 450 K, the cycles represent the observed intensities (black), and the solid line is the calculated profile (red). The difference between the observed and calculated intensities is shown at the bottom (blue). The vertical bars indicate the expected Bragg reflection positions (black). The peak indicated by the blue dashed frame is a magnetic peak of YbMnSb$_2$, and the inset shows the Mn magnetic structures of YbMnSb$_2$: *C*-type AFM with moments along *c*; (b) The waterfall plots of the temperature-dependent neutron diffraction profiles for YbMnSb$_2$. (c) Isothermal contour image of the zero-field neutron diffraction pattern of YbMnSb$_2$ over the temperature range from 10 K to 450 K.

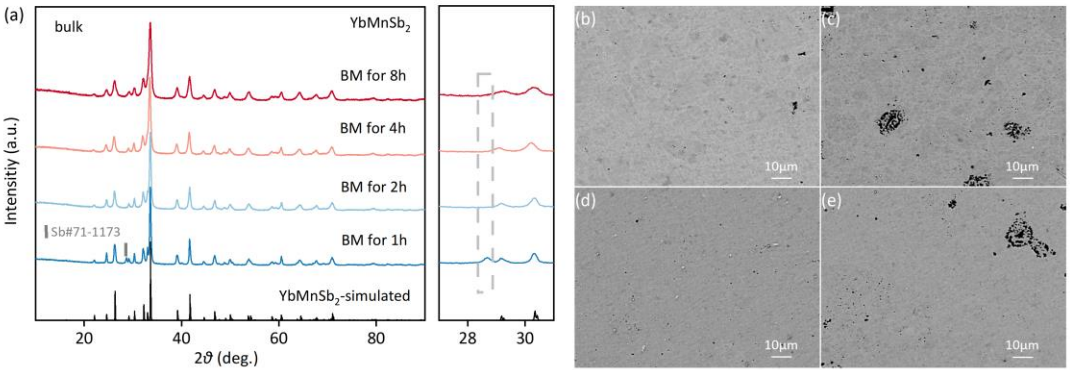

Figure 3. (a) Room-temperature powder X-ray diffraction patterns and (b-e) back-scattered SEM of YbMnSb$_2$ samples synthesized using the BM+SPS method.

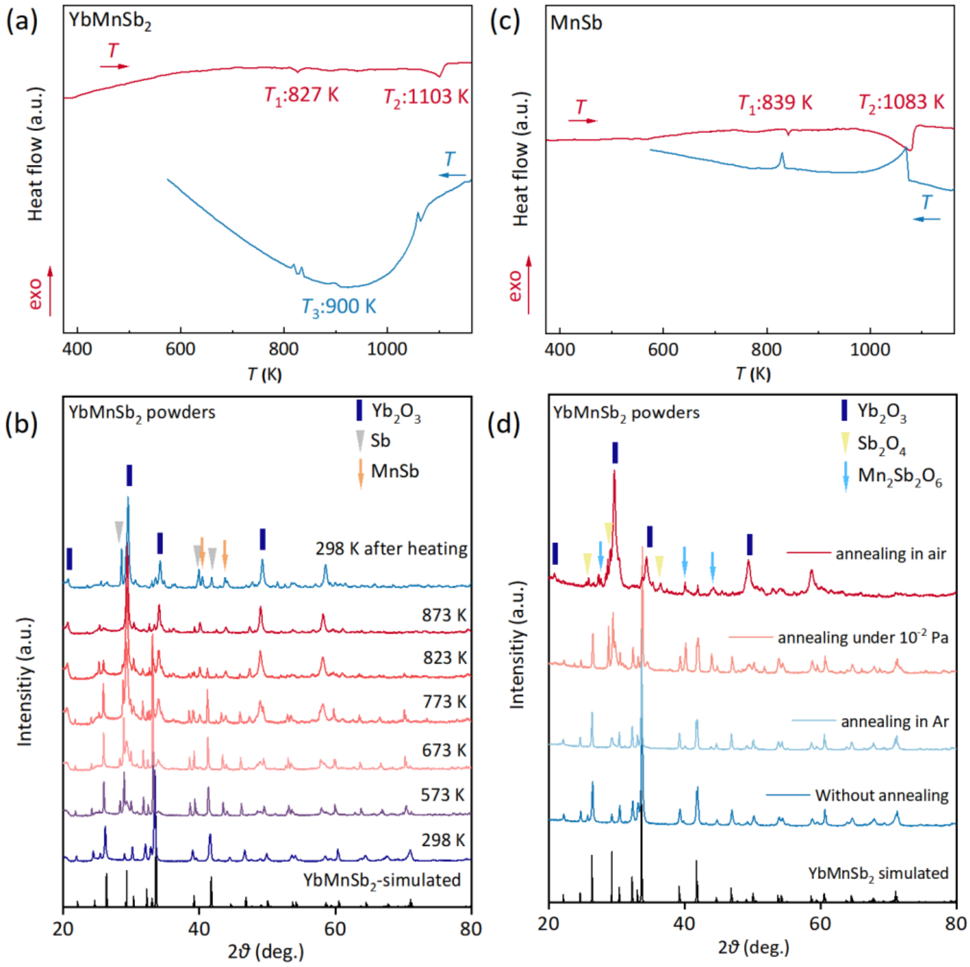

Figure 4. (a) DSC curves for polycrystalline YbMnSb$_2$ powders from 373 to 1173 K with a heating rate of 10 K/min; (b) In-situ XRD patterns for YbMnSb$_2$ from 298 to 873 K (The dark blue rectangular represent the characteristic peaks of Yb$_2$O$_3$, the Gray triangle represent the characteristic peaks of Sb, the orange arrow represent the characteristic peaks of MnSb); (c) DSC curves for polycrystalline MnSb powders from 373 to 1173 K with a heating rate of 10 K/min; (d) XRD patterns for YbMnSb$_2$ annealed in a sealed quartz tube at 873 K for 3 h under different atmospheres (In the air, Ar, and low-vacuum of around 10^{-2} Pa, respectively), the dark blue rectangular represent the characteristic peaks of Yb$_2$O$_3$, the yellow triangle represent the characteristic peaks of Sb$_2$O$_4$, the light blue arrow represent the characteristic peaks of Mn$_2$Sb$_2$O$_6$.

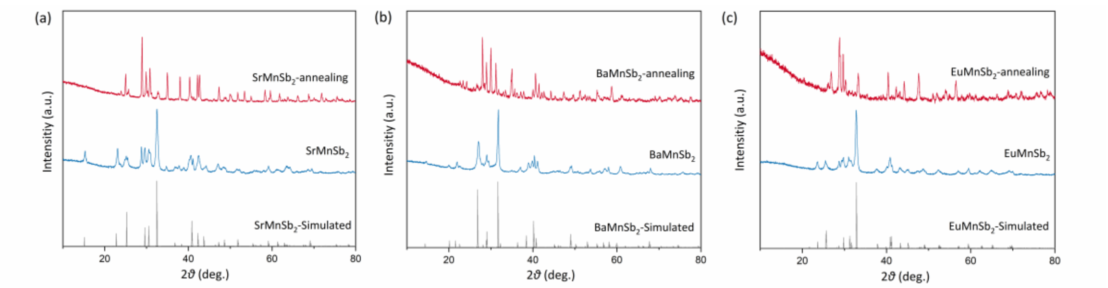

Figure 5. Room-temperature powder X-ray diffraction patterns of (a) $SrMnSb_2$; (b) $BaMnSb_2$; (c) $EuMnSb_2$ samples synthesized using the BM+SPS method and annealing in a sealed quartz tube at 873 K for 3 h under low-vacuum.

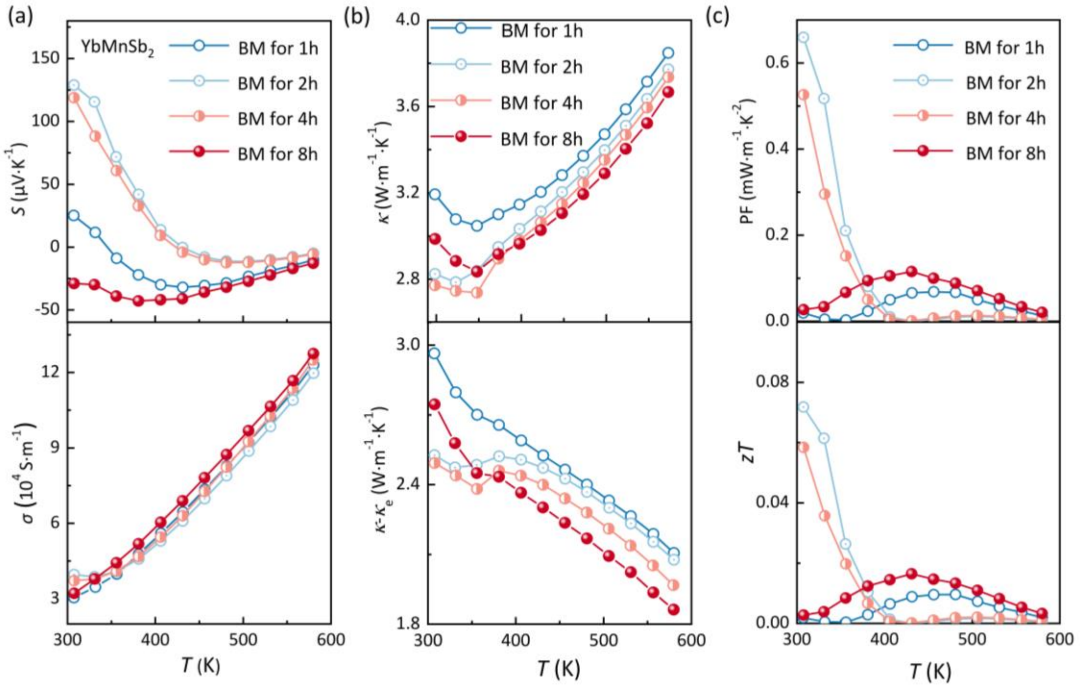

Figure 6. Temperature dependences of (a) electrical conductivity σ, Seebeck coefficient S; (b) total thermal conductivity κ, κ - κ_e; (c) power factor PF and zT values for bulk $YbMnSb_2$ (BM for 1, 2, 4, and 8 hours, respectively).

[[Graphical Abstract]]

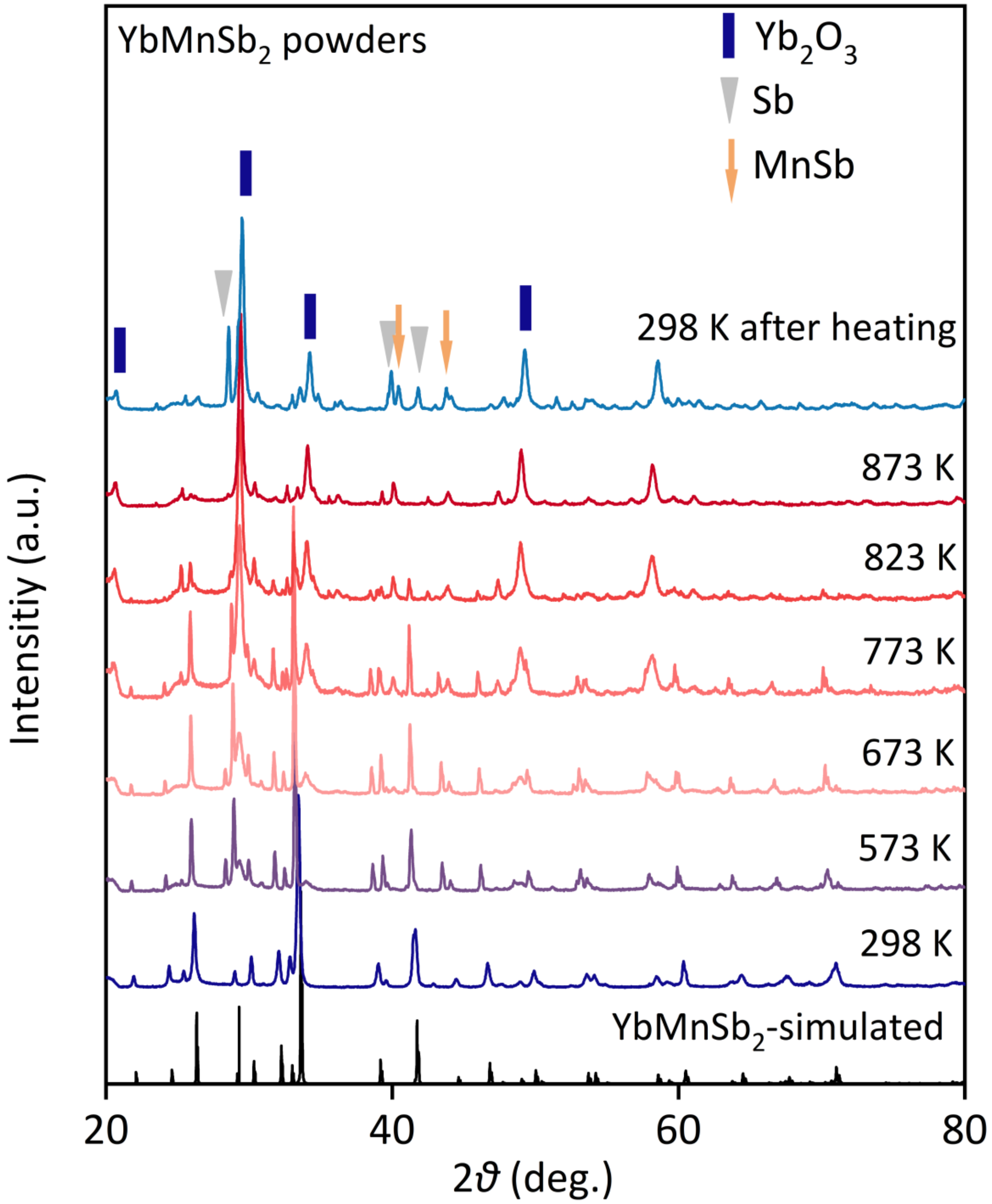

Supporting Information

Synthesis and thermal stability of topological semimetal *R*MnSb$_2$ (*R* = Yb, Sr, Ba, Eu)

Shuo Liu[a], Airan Li[a], Xiaowen Hao[b,c], Mengzhao Chen[a], Yi Huang[a], Yinde Yu[b,c], Chin-Wei Wang[d], Qingyong Ren[b,c,*], Tiejun Zhu[a,*] Chenguang Fu[a,*]

[a]State Key Laboratory of Silicon and Advanced Semiconductor Materials, School of Materials Science and Engineering, Zhejiang University, Hangzhou 310058, China

[b]Spallation Neutron Source Science Center, Dongguan 523803, China

[c]Institute of High Energy Physics, Chinese Academy of Sciences, Beijing 100049, China

[d]National Synchrotron Radiation Research, Hsinchu 300092, Taiwan

[*]Email: chenguang_fu@zju.edu.cn; zhutj@zju.edu.cn; renqy@ihep.ac.cn

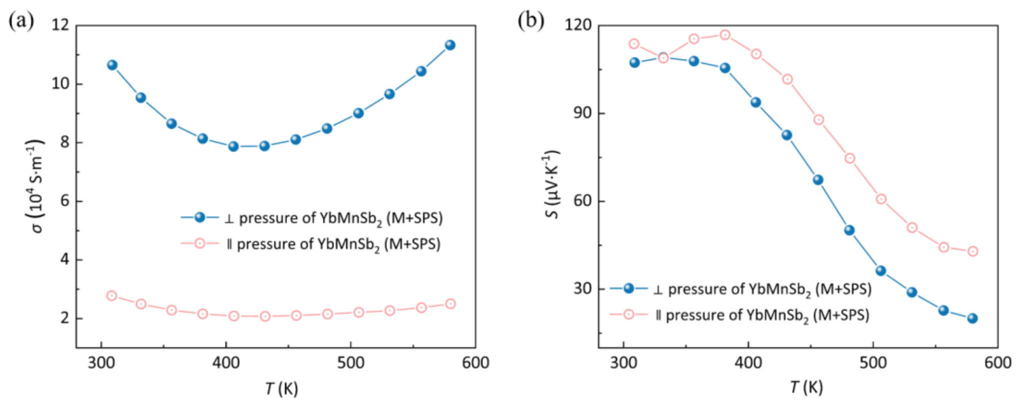

Figure S1. Temperature dependences of (a) electrical conductivity σ, (b) Seebeck coefficient S along different directions for YbMnSb$_2$ fabricated using M+SPS method.

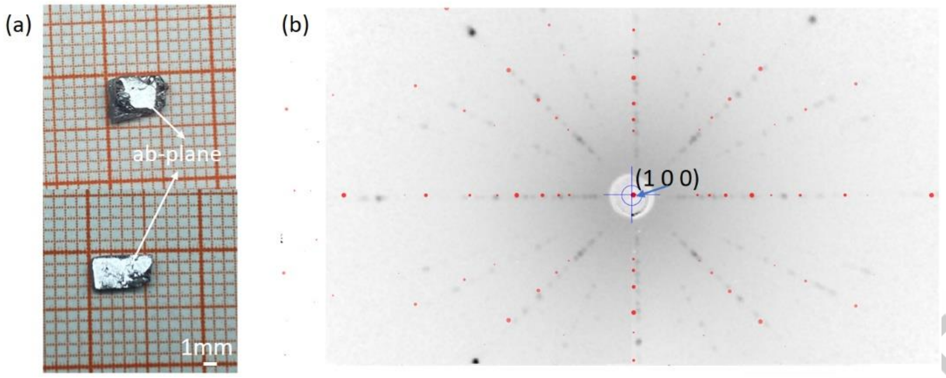

Figure S2. (a) Optical images of the single crystal with a clear cleavage plane; (b) The Laue diffraction pattern of $YbMnSb_2$ single crystal.

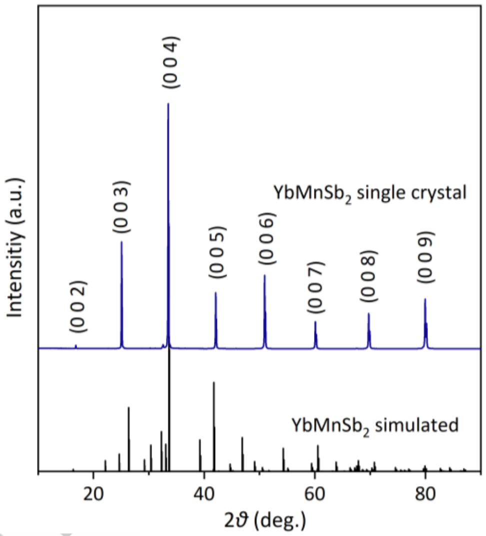

Figure S3. XRD pattern for $YbMnSb_2$ single crystal.

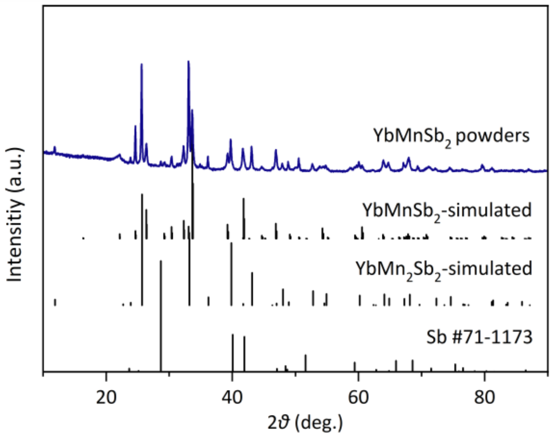

Figure S4. XRD pattern for powders ground from the as-grown $YbMnSb_2$ single crystal.

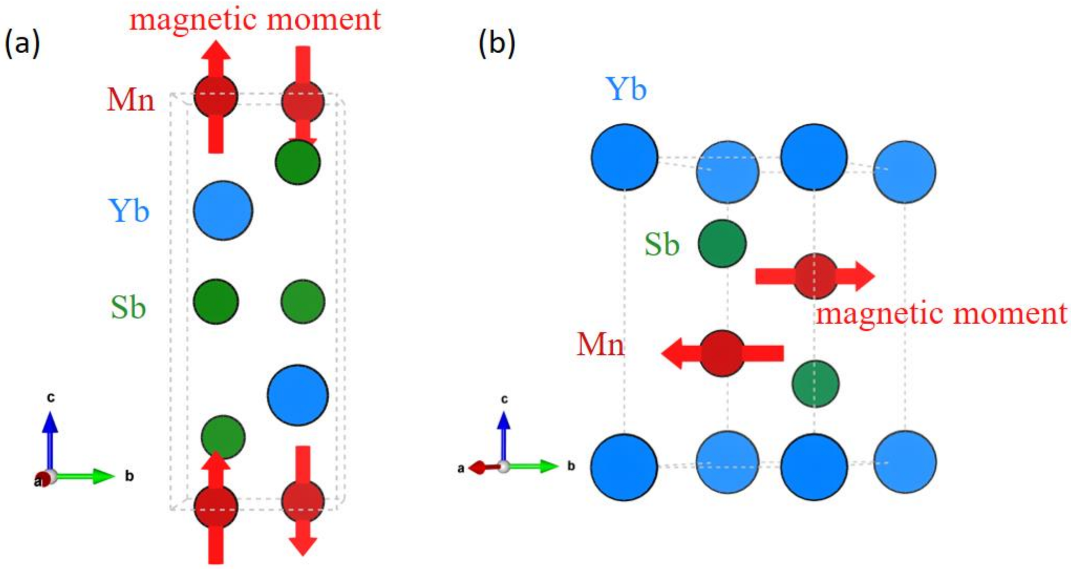

Figure S5. The Mn magnetic structures of $YbMnSb_2$ (a) and $YbMn_2Sb_2$ (b).

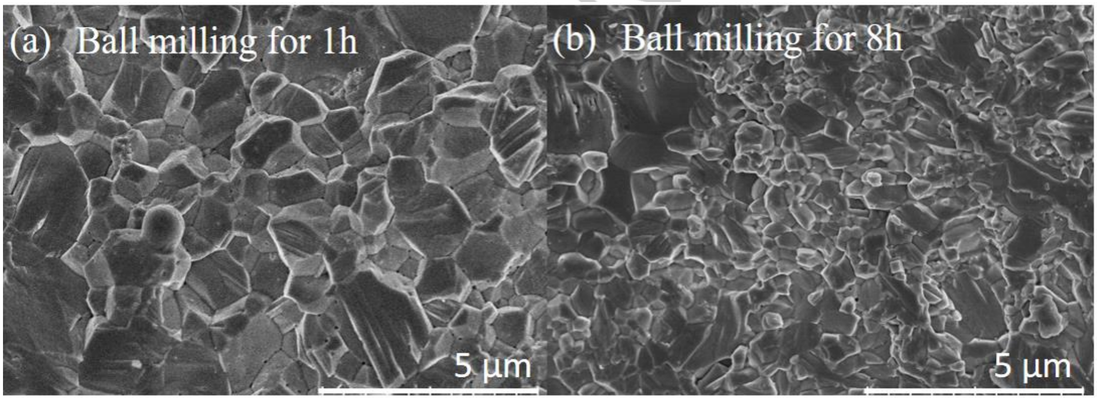

Figure S6. SEM images of fractured surfaces for samples ball milling for 1h (a) and 8h (b).

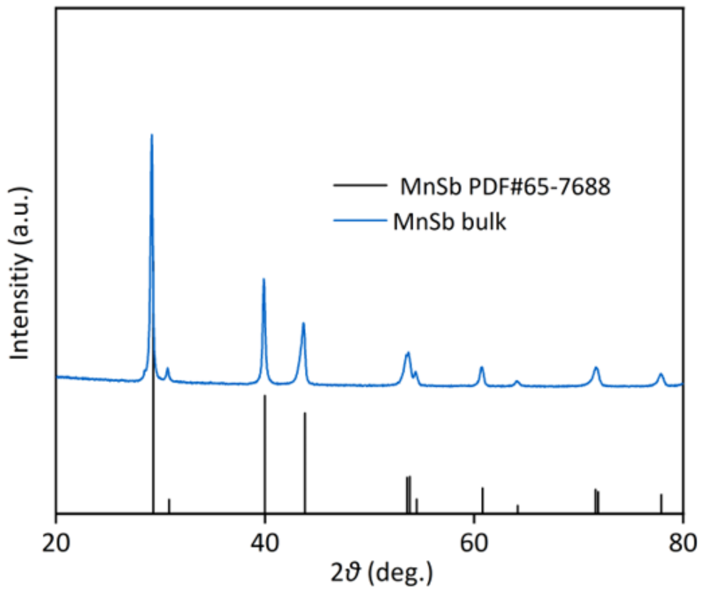

Figure S7. XRD pattern for bulk MnSb.

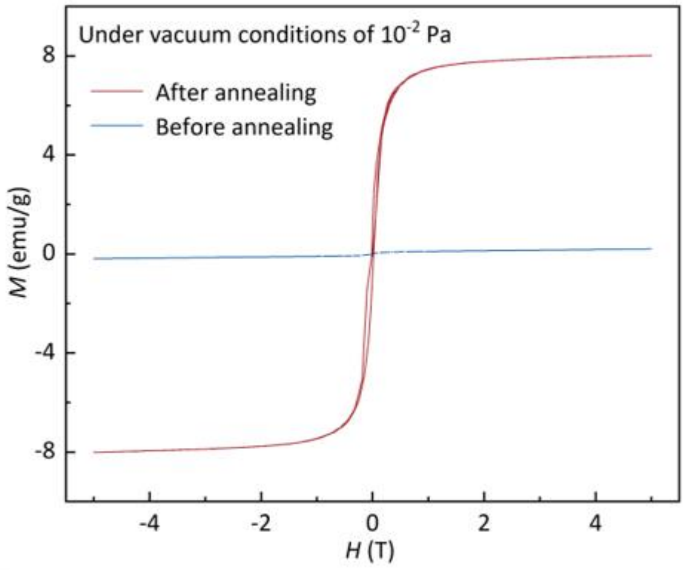

Figure S8. *M*-*H* curves of the $YbMnSb_2$ sample before and after annealing at a low vacuum of around 10^{-2} Pa.

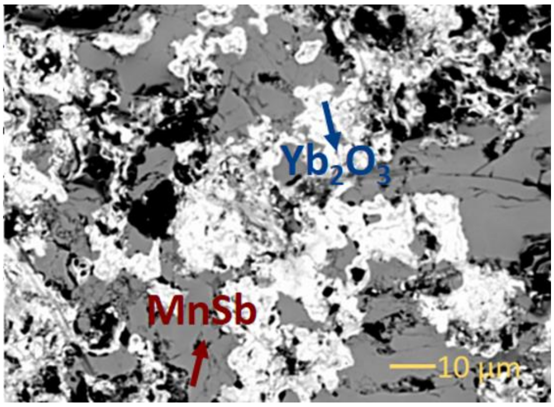

Figure S9. Backscattered electron (BSE) image of the YbMnSb$_2$ sample after annealing under a low vacuum of around 10^{-2} Pa.

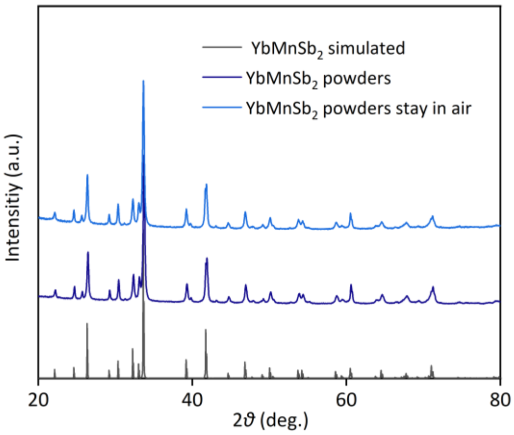

Figure S10. X-ray diffraction patterns of YbMnSb$_2$ powders before and after staying in the air for five days.

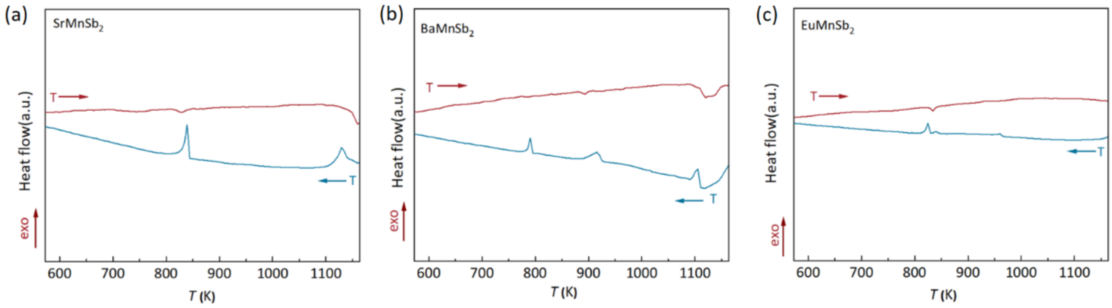

Figure S11. DSC curves for polycrystalline (a)SrMnSb$_2$; (b) BaMnSb$_2$ and (c) EuMnSb$_2$ powders from 373 to 1173 K with a heating rate of 10 K/min.

Table S1. The EPMA results of different parts for Figure S9.

EPMA of selected areas	Atomic % of O	Atomic % of Sb	Atomic % of Mn	Atomic % of Yb
Gray part 1	5.75	46.20	46.34	1.71
Gray part 2	4.55	46.36	48.92	0.13
White part 1	60.65	1.36	1.59	36.40
White part 2	57.94	3.05	2.47	36.54